



Flow distribution in parallel microfluidic networks and its effect on concentration gradient

Cyprien Guermonprez, Sébastien Michelin, Charles N. Baroud

► To cite this version:

Cyprien Guermonprez, Sébastien Michelin, Charles N. Baroud. Flow distribution in parallel microfluidic networks and its effect on concentration gradient. *Biomicrofluidics*, 2015, 9 (5), pp.054119. 10.1063/1.4932305 . hal-01246210

HAL Id: hal-01246210

<https://polytechnique.hal.science/hal-01246210>

Submitted on 18 Dec 2015

HAL is a multi-disciplinary open access archive for the deposit and dissemination of scientific research documents, whether they are published or not. The documents may come from teaching and research institutions in France or abroad, or from public or private research centers.

L'archive ouverte pluridisciplinaire **HAL**, est destinée au dépôt et à la diffusion de documents scientifiques de niveau recherche, publiés ou non, émanant des établissements d'enseignement et de recherche français ou étrangers, des laboratoires publics ou privés.

Flow distribution in parallel microfluidic networks and its effect on concentration gradient

Cyprien Guermonprez, Sébastien Michelin, and Charles N. Baroud

Citation: **Biomicrofluidics** **9**, 054119 (2015); doi: 10.1063/1.4932305

View online: <http://dx.doi.org/10.1063/1.4932305>

View Table of Contents: <http://scitation.aip.org/content/aip/journal/bmf/9/5?ver=pdfcov>

Published by the AIP Publishing

Articles you may be interested in

[A novel microfluidic flow focusing method](#)

Biomicrofluidics **8**, 054120 (2014); 10.1063/1.4899807

[Simulations of DNA stretching by flow field in microchannels with complex geometry](#)

Biomicrofluidics **8**, 014106 (2014); 10.1063/1.4863802

[Label-free viscosity measurement of complex fluids using reversal flow switching manipulation in a microfluidic channel](#)

Biomicrofluidics **7**, 044106 (2013); 10.1063/1.4816713

[High-throughput particle manipulation by hydrodynamic, electrokinetic, and dielectrophoretic effects in an integrated microfluidic chip](#)

Biomicrofluidics **7**, 024106 (2013); 10.1063/1.4795856

[Microfluidic three-dimensional hydrodynamic flow focusing for the rapid protein concentration analysis](#)

Biomicrofluidics **6**, 024132 (2012); 10.1063/1.4730332

TREK
www.trekinc.com

HIGH-VOLTAGE AMPLIFIERS AND ELECTROSTATIC VOLTMETERS

ENABLING RESEARCH AND INNOVATION IN DIELECTRICS, MICROFLUIDICS, MATERIALS, PLASMAS AND PIEZOS

Flow distribution in parallel microfluidic networks and its effect on concentration gradient

Cyprien Guermonprez, Sébastien Michelin, and Charles N. Baroud^{a)}

*LadHyX & Department of Mechanics, Ecole Polytechnique, CNRS,
91128 Palaiseau, France*

(Received 17 June 2015; accepted 22 September 2015; published online 6 October 2015)

The architecture of microfluidic networks can significantly impact the flow distribution within its different branches and thereby influence tracer transport within the network. In this paper, we study the flow rate distribution within a network of parallel microfluidic channels with a single input and single output, using a combination of theoretical modeling and microfluidic experiments. Within the ladder network, the flow rate distribution follows a U-shaped profile, with the highest flow rate occurring in the initial and final branches. The contrast with the central branches is controlled by a single dimensionless parameter, namely, the ratio of hydrodynamic resistance between the distribution channel and the side branches. This contrast in flow rates decreases when the resistance of the side branches increases relative to the resistance of the distribution channel. When the inlet flow is composed of two parallel streams, one of which transporting a diffusing species, a concentration variation is produced within the side branches of the network. The shape of this concentration gradient is fully determined by two dimensionless parameters: the ratio of resistances, which determines the flow rate distribution, and the Péclet number, which characterizes the relative speed of diffusion and advection. Depending on the values of these two control parameters, different distribution profiles can be obtained ranging from a flat profile to a step distribution of solute, with well-distributed gradients between these two limits. Our experimental results are in agreement with our numerical model predictions, based on a simplified 2D advection-diffusion problem. Finally, two possible applications of this work are presented: the first one combines the present design with self-digitization principle to encapsulate the controlled concentration in nanoliter chambers, while the second one extends the present design to create a continuous concentration gradient within an open flow chamber. © 2015 AIP Publishing LLC.

[<http://dx.doi.org/10.1063/1.4932305>]

I. INTRODUCTION

As the complexity of microfluidic devices increases, with several branching channels connected to a single source, some surprising observations are found on the flow distribution in these networks. It is well known that multiphase flows can exhibit complex behavior around a loop^{1,2} or that a viscosity contrast can lead to an unstable flow distribution at a bifurcation.³ What is less well documented is how a single phase flow distributes through a network of channels, in part because low Reynolds number (Re) flows are assumed to follow simple symmetric patterns. Nevertheless, we have often observed an uneven distribution of fluid in networks of channels even for the simplest situations.

Understanding this flow distribution is especially important for understanding and predicting the transport of molecules through a set of parallel channels. Indeed, the low value of the Reynolds number typical in microfluidics inhibits efficient mixing of different species. This in

^{a)}Author to whom correspondence should be addressed. Electronic mail: baroud@ladhyx.polytechnique.fr

turn places significant obstacles to the generation of controlled concentration contrasts, for example, for cell migration,⁴ protein crystallisation tests,⁵ or enzyme kinetics measurements.^{6,7} In response to this constraint, several methods have been suggested for generating controllable concentration gradients in microchannels, taking advantage of the reproducible laminar flows. For example, successive fusions of highly concentrated initial droplets with droplets of pure solvent have been shown to produce a train of droplets with varying conditions.^{8–10} Taylor-Aris dispersion was also used to establish a streamwise concentration gradient, which was then encapsulated into individual droplets.¹¹

In single-phase flows, several devices combining solute diffusion with a flow in a network of channels have been developed in order to tailor a concentration profile of one or several solutes.^{12–14} In those systems, the distribution of the diffusing species is determined by the relative importance of advection by the solvent's flow and diffusion of the solute,¹² which can be used to tune the concentration profile in a given device. Indeed, although the flow distribution does not depend on the total flow rate for low Re flows, the time available for diffusion to operate will decrease with higher flow rates. This has been shown to play a major role in determining the final concentration gradient.¹²

Few studies have modeled the concentration distribution within such devices analytically¹³ or numerically.^{15,16} Here, we present a new modeling approach that provides theoretical foundation for the physical understanding of the gradient generation control while focusing on a particular gradient-generating device initially introduced by Selimović *et al.*,¹⁶ as shown in Fig. 1(a). Compared with the well known tree-like geometry,¹² this device allows the production of a gradient on a smaller footprint and in a more robust manner. We extend the observations of Selimović *et al.* by providing a simplified physical model based on two dimensionless parameters. We show that the solute gradient can be tailored by controlling these two

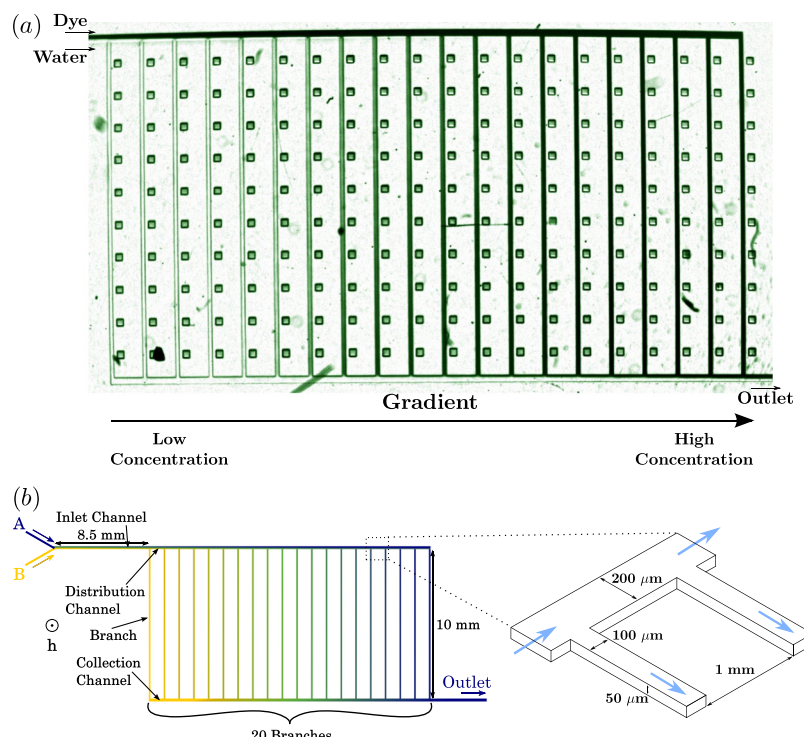


FIG. 1. (a) Experimental image of the ladder network with a dye concentration. Two streams (dye and pure water) are injected from the top-left region and flow into the network, before exiting from the outlet at the bottom-right. A concentration gradient is formed in the parallel vertical channels. (b) Microfluidic network structure with dimensions. For flow rate measurements, a 10 branches device is used, while for concentration profiles measurement, a 20 branches ladder network is used.

parameters, and we provide design tools for adapting the device to more complex microfluidic networks.

After describing the experimental parameters in Section II, we model the flow distribution in the parallel ladder network in Section III A. This distribution displays a non-trivial U-shaped velocity whose depth is determined by a single geometric parameter that describes the ratio of fluidic resistances in different parts of the network. Once the flow-rate distribution is known, the solute transport is modeled by solving an advection-diffusion model in Section III B. This introduces a second nondimensional parameter, the Péclet number (Pe), and it is the combination of these two dimensionless parameters that determines the global solute profile in the network. The theoretical predictions of Section IV are then confirmed using experimental measurements. Finally, we propose, in Section V, two examples of how such a device can be extended to more directly applicable situations, before concluding in Section VI.

II. EXPERIMENTAL METHODS

The detailed microchannel geometry is shown in Fig. 1(b). Two independent solutions are injected at entrances A and B and flow side-by-side in the inlet channel before they are distributed through the distribution channel between the branches. The flows are controlled with a syringe pump (Cetoni Nemesys), or through a pressure controller (Fluigent MFCS), and the behavior within the microchannels is observed through an inverted microscope (Nikon TE-2000) as described below.

A. Chip microfabrication

All experiments were conducted in PDMS microchannels (Dow Corning Sylgard 184) plasma-sealed onto glass slides. The mold fabrication process was based on dry film photoresist soft lithography techniques, as described in detail by Fradet *et al.*¹⁷ The channel surfaces were untreated for most experiments. However, hydrophobic surfaces were obtained for the experiments of Section V by filling the device with an electronic coating EG-1720 (Acota Ltd, Knights Way, Shrewsbury, UK) and then baking at 110 °C. Two chip designs are used: 15 μm height for flow rates measurements and 50 μm height for experiments involving concentration gradients.

B. Flow rate measurements

The flow rate in the distribution channel and branches was measured using non diffusing tracer particles (LifeTechnologies, 1.0 μm FluoSpheres) diluted in aqueous solutions. The solution was injected at 1 $\mu\text{l}/\text{min}$ in both entrances and filmed using Photron Fast Camera at 30 \times magnification. In steady flow, microparticles follow the streamlines, which can then be visualized using image superposition as presented in Fig. 2.

At each branching node, a clear separating streamline is visible between the fluid that is diverted into the side branch and the fluid that continues through the distribution channel (dashed line in Fig. 2). The upstream distance between the bottom wall and the separation line is denoted as e_i for node i . Away from the branching site, the depth-averaged Hele-Shaw flow is uniform along the channel width. Hence, conservation of mass at node i provides a relation between e_i and the flow rate within the distribution channel upstream (Q_i) and downstream (Q_{i+1})

$$1 - \frac{e_i}{w} = \frac{Q_{i+1}}{Q_i} \quad 1 \leq i \leq N - 1, \quad (1)$$

where w is the width of the distribution channel. Therefore, the flow rate $(Q_i)_{i=1\dots N}$ along the distribution channel is obtained by measuring $(e_i)_{i=1\dots N}$ and by noting that $Q_1 = Q_A + Q_B$. Finally, the flow rate distribution $(q_i)_{i=1\dots N}$ in the parallel branches is computed using mass conservation as $q_i = Q_i - Q_{i+1}$, noting that $q_N = Q_N$.

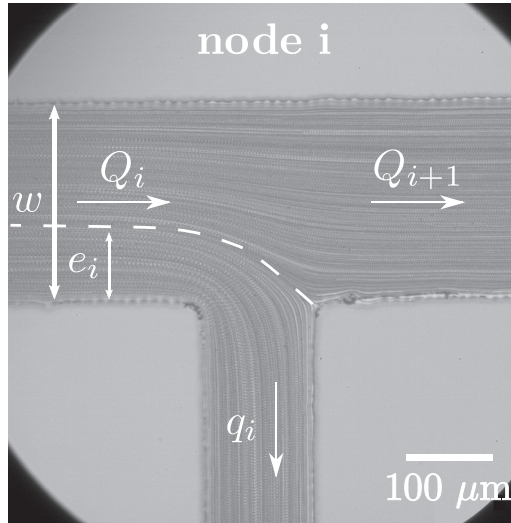


FIG. 2. Stack projection of 122 images of micro particles flowing through node i . e_i is the distance from the lower wall to the separation line (white dashed) between the fluid that gets into a side branch and the remaining flow that continues through the distribution channel.

C. Concentration gradients measurements

To quantify the concentration gradients generated in the chip, a 10 mmol 2,6-dichlorophenolindophenol (DCPIP) solution is injected at entrance A, while pure water is pumped at inlet B. Q_A and Q_B are always identical and range from 0.5 $\mu\text{l}/\text{min}$ to 20 $\mu\text{l}/\text{min}$. DCPIP has a diffusion coefficient⁷ $D = 0.77 \times 10^{-9} \text{ m}^2/\text{s}$.

The concentration levels are obtained from measurements of the light absorbance through the blue DCPIP solution. The local absorbance \mathcal{A} is related through Beer's law to the local concentration of absorbing species (here DCPIP), noted C (in mol/m^3)

$$\mathcal{A} = \epsilon h C \quad \text{with} \quad \mathcal{A} = -\log \frac{I}{I_0}, \quad (2)$$

with ϵ the molar extinction coefficient (in $\text{mol}^{-1} \text{ m}^{-1}$) of DCPIP and h (in m) the optical path length of light, which corresponds to the channel height. I and I_0 are the measured intensity and the background intensity, respectively. Experimentally, I_0 corresponds to the intensity through pure water flow ($C = 0 \text{ mM}$). In practice, the local concentration C is obtained by measuring the local intensity I and comparing it with I_0 and a reference value I_{ref} that corresponds to the undiluted DCPIP concentration C_{ref} . This yields

$$\frac{C}{C_{\text{ref}}} = \frac{\log \frac{I}{I_0}}{\log \frac{I_{\text{ref}}}{I_0}}. \quad (3)$$

III. FLOW AND TRANSPORT MODELS

A model for the flow distribution and transport of solute through the device is developed to allow for a systematic investigation of the influence of flow rate and channel geometry on the gradient profile in the branches. We first present a hydrodynamic model for the flow rate distribution, before turning to the solute advection-diffusion problem.

A. Hydrodynamic resistance network

When the depth and width of each microchannel are small in comparison with its length, a 1D-hydrodynamic resistance model can be used, namely, by relating through the hydrodynamic

Ohm's law, $\Delta P = R_{hyd}Q$, the pressure loss ΔP between the channel segment's inlet and outlet to the flow rate Q through that segment. The hydrodynamic resistance of a channel with rectangular cross-section is given by $R_{hyd} = a(w/h)R_{hyd}^*$, with $R_{hyd}^* = \mu L/w^2 h^2$, μ the dynamic fluid viscosity, and $a(w/h)$ a geometric factor.¹⁸ L , w , and h are the channel length, width, and height, respectively ($h < w$).

Thus, the microfluidic network can be represented as a hydrodynamic resistance network (Fig. 3(a)), where p_i (respectively, p_i^f) is the pressure at node i in the distribution (respectively, collection) channels. Similarly, Q_i and Q_i^f are the flow rates upstream of node i in the distribution and collection channels. The distribution and collection channels have the same geometric characteristics, and the side branches are all identical. We note R the hydrodynamic resistance between two nodes of the distribution or collection channel segment and R_b the hydrodynamic resistance of each branch. Kirchhoff's law applied between nodes $i-1$ and i (see Fig. 3(a)) yields

$$R_b(q_i - q_{i-1}) = R(Q_i^f - Q_i) \quad \text{for } 2 \leq i \leq N, \quad (4)$$

and from mass conservation,

$$Q_1 = \sum_{k=i}^N q_k + \sum_{k=1}^{i-1} q_k \quad (5)$$

for all $1 \leq i \leq N$. Equations (4) and (5) can be recast in terms of the normalized flow rate $\tilde{q}_i = q_i/Q_1$ in the branches

$$\tilde{q}_i - \tilde{q}_{i-1} = \frac{R}{R_b} \left(\sum_{k=1}^{i-1} \tilde{q}_k - \sum_{k=i}^N \tilde{q}_k \right) \quad \text{for } 2 \leq i \leq N, \quad (6)$$

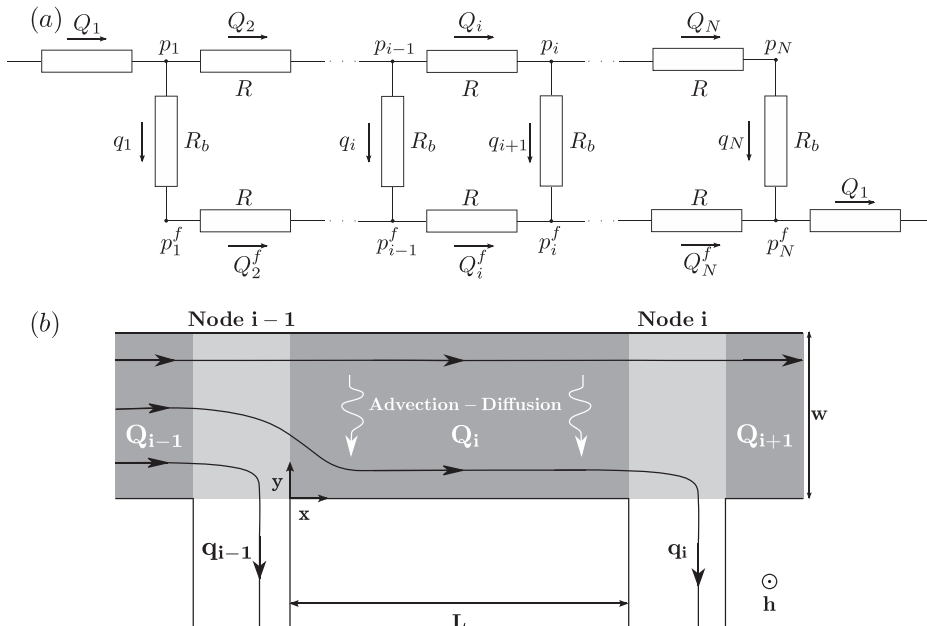


FIG. 3. (a) Equivalent resistance network: R and R_b are the hydrodynamic resistances of a segment between two nodes and of a branch, respectively. p_i and p_i^f are the pressure at the entrance and the exit of branch i , respectively. The flow rates in the branches are written q_i . Q_i and Q_i^f correspond, respectively, to distribution channel and collection channel inter nodes flow rates, while Q_1 is the global inlet flow rate. (b) Schematic of an inlet section between nodes $i-1$ and i . Advective transport dominates near each node (light grey zones), while the solute distribution between two nodes results from a balance between advection and cross-flow diffusion (dark grey zones).

$$\sum_{k=1}^N \tilde{q}_k = 1. \quad (7)$$

The previous system is controlled by a single parameter, R/R_b , which solely depends on the network's geometry

$$\frac{R}{R_b} = \frac{a\left(\frac{w}{h}\right)}{a\left(\frac{w_b}{h}\right)} \left(\frac{L}{L_b}\right) \left(\frac{w_b}{w}\right)^2, \quad (8)$$

with L_b , w_b , and h_b the length, width, and height of the branches. For a given geometry (or a given R/R_b), the normalized branch and distribution channel flow rates, \tilde{q}_i and \tilde{Q}_i with $1 \leq i \leq N$, are computed from Eqs. (6) and (7), and

$$\tilde{Q}_i = \sum_{k=i}^N \tilde{q}_k. \quad (9)$$

B. Solute advection-diffusion

Because of the discrete nature of the network, the solute dynamics can be modeled by distinguishing what happens within a channel segment and in the vicinity of a branching node. The channel and branch heights being small, diffusion is expected to act quickly in that direction and a two-dimensional model is assumed for the depth-averaged concentration and velocity. Away from the branching nodes, the depth-averaged flow velocity within the segment is uniform. Because the length of the segment is large compared to its width, we neglect streamwise diffusion. As a result, the relative solute concentration, $\tilde{C} = C/C_{\text{ref}}$, is modeled by the following two-dimensional advection-diffusion equation within the segment

$$\text{Pe} \tilde{Q}_i \frac{\partial \tilde{C}}{\partial \tilde{x}} = \frac{\partial^2 \tilde{C}}{\partial \tilde{y}^2}, \quad (10)$$

with $\tilde{x} = x/L$ and $\tilde{y} = y/w$, the non-dimensional coordinates. The Péclet number,

$$\text{Pe} = \frac{Q_1 w}{DLh}, \quad (11)$$

is the ratio of the typical diffusion time across the distribution channel, w^2/D , to the advection time scale along the entire channel $Q_1/(wLh)$, with D the solute diffusion coefficient. Equation (10) is solved using finite differences and a Crank-Nicholson scheme for each segment.

Near a branching node, the solute dynamics is dominated by the flow reorganization in that region (Figure 2), and because of the small extent of that region, diffusion can be neglected while the flow reorganizes. The solute concentration profile downstream from node i is therefore directly obtained by stretching the upstream profile in the cross-stream direction to account for the spreading of the streamlines in the distribution channel. In the side branch, diffusion quickly homogenizes the solute concentration downstream of the branching node so that the measured concentration can be defined as its average value.

For $Q_A = Q_B$, the solute concentration distribution at the entrance of the inlet channel is a centered Heaviside function. The evolution of the concentration profile along the inlet channel is determined from Eq. (10). Then, the solute concentration profile downstream of node i and its value in the i -th branch are computed using the method described above (light grey section

in Fig. 3(b)), while the evolution of the concentration profile in the distribution channel is computed between two nodes using Eq. (10) (dark grey section in Fig. 3(b)).

IV. RESULTS AND DISCUSSION

In the following, we compare the results of our models (Section III) to our experimental measurements (Section II) and use these models to obtain some important physical insight on the role of flow rate and network geometry in tailoring the concentration gradients between the branches.

A. Flow rate distribution

For a given network geometry (i.e., given R/R_b), the distribution profile of flow rates in the parallel branches is obtained from Eqs. (6) and (7). The flow rate displays a U-shaped distribution, with the highest flow rates in the first and last branches and lower values in the middle of the ladder, as plotted in Fig. 4(a) for three values of R/R_b . A larger contrast between the maximum flow rates and the flow rate in the middle branches is observed when R/R_b is increased. For $R/R_b = 0.43$, 85% of the global inlet flux Q_1 flows through the first two and last two branches. This quantity decreases to 46% for $R/R_b = 0.043$. At $R/R_b = 0.0043$, the fluid is more equally distributed between the branches with a low contrast $|q_{\max} - q_{\min}|/Q_1 \leq 2\%$. Hence, high branch resistances give more homogeneous flow rate distributions than low branch resistances.

The U-shaped profile can be explained by calculating p_i and p_i^f , the values of the inlet and outlet pressures for each branch (Fig. 4(c)). Applying the conservation of flow rate at node i in the distribution or collection channels, as well as Ohm's law, gives

$$p_{i+1} - 2p_i + p_{i-1} = Rq_i, \quad (12)$$

$$p_{i+1}^f - 2p_i^f + p_{i-1}^f = -Rq_i. \quad (13)$$

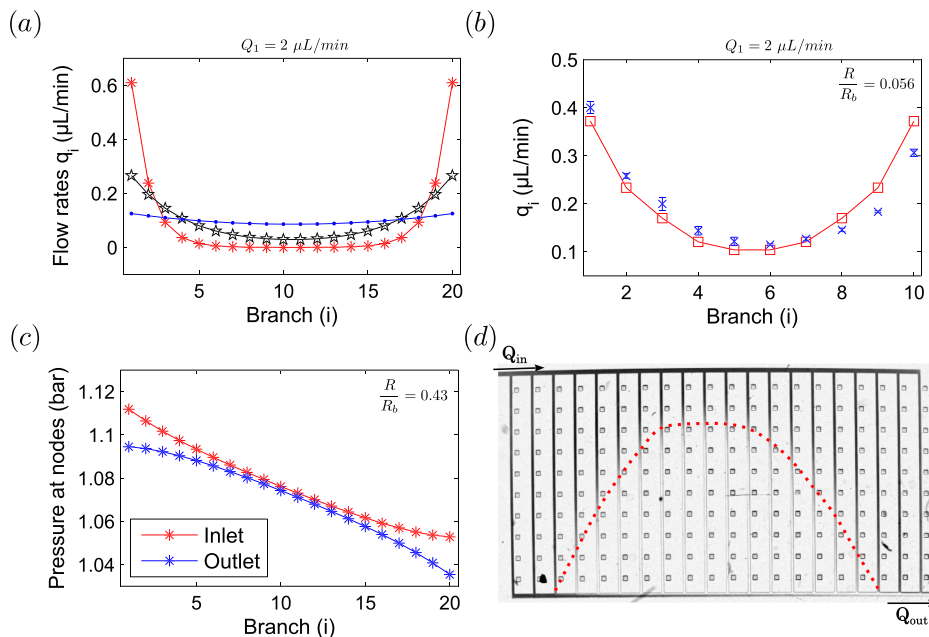


FIG. 4. (a) Simulated flow rate distributions for three different geometries. In each case, the branch resistance is changed such that the ratio $\frac{R}{R_b}$ is varying. (b) Comparison between numerical (\square) and experimental (\times) branch flow rate distribution for a ten branches device with $Q_A = Q_B = 1 \mu\text{L}/\text{min}$ and $\frac{R}{R_b} = 0.056$. (c) Pressures at nodes $(P_i)_{i=1 \dots N}$ and $(P_i^f)_{i=1 \dots N}$ for $\frac{R}{R_b} = 0.43$. (d) Image of a device filling process with only one species: DCPIP at 6mM .

Equations (12) and (13) show that the inlet and outlet pressure distributions have opposite convexity: since q_i is defined as positive in the notations of Fig. 3(a), the inlet (respectively, outlet) pressure distribution is convex (respectively, concave), a result confirmed in Fig. 4(c). The branch flow rate is simply proportional to the difference between the two pressures at each i ; thus, the flow will always be higher at the edges of the ladder and smaller in the center. This result contrasts with the linear pressure drop along a simple channel with no side exits.

This theoretical prediction is confirmed experimentally for $R/R_b = 0.056$ (Fig. 4(b)). The experimental flow rates, which are obtained from the method described in Section II, are in very good agreement with the model predictions in the first channels. In the last channels, the accumulation of measurement errors leads to a discrepancy with the model, although the agreement remains good.

The signature of this velocity profile is best visualised by injecting a colored solution into a ladder filled with pure water. The filling process occurs sooner near the beginning and end of the ladder network than in the central region, as shown on the snapshot of Fig. 4(d) and in the accompanying movie S1.²⁶ This distribution of flow rate has an important practical consequence: changing the contents in the device is therefore limited by the time required to fill the central region and would require a volume greater than the total volume in the device.

B. Concentration gradient profiles

The flow rate distribution in the branches depends on a single geometric parameter. In addition to this flow rate distribution within the ladder, the solute concentration profile also depends on the relative importance of advection and diffusion, measured by the Péclet number, which now acts as the second dimensionless number controlling the gradient formation process. Experimentally, Pe can be adjusted by changing the inlet flow rate Q_1 for a fixed channel geometry and diffusing species. To simplify the analysis, we first analyze the concentration gradient dependence on the Péclet number for a fixed geometry, and then we integrate both parameters to obtain a full map of the accessible concentration gradient profiles.

Figure 5 shows the resulting concentration distribution for $R/R_b = 0.043$ as a function of Pe. Three main types of profiles can be distinguished, referred to in the following as “flat,” “gradient,” and “step” concentration profiles. The flat profiles are obtained for low Pe, when diffusion is sufficiently fast to homogenize the concentration in the distribution channel after a few nodes. The step profile is obtained for large Pe, when diffusion is almost negligible: the first branches are filled with pure solvent injected at entrance A, while the last ones are filled with pure solute solution. Finally, gradient profiles correspond to the intermediate regime, when both advection and diffusion are significant.

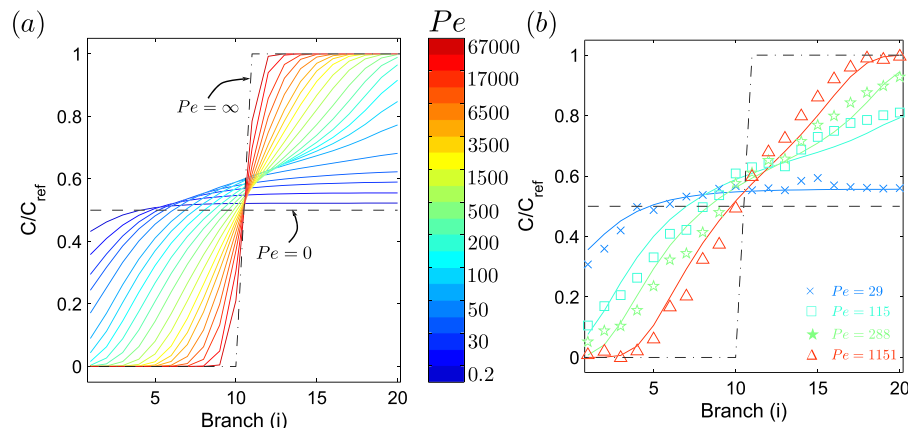


FIG. 5. (a) Concentration profiles for Péclet numbers from 0.2 to 6.7×10^4 for a fixed geometry $R/R_b = 0.043$, obtained from the numerical simulation (Section III). The extreme “flat” and “step” gradients are also plotted (dashed and dotted-dashed curves). (b) Comparison between the experimental data and the numerical model for four different flow rates: $Q_1 = 1, 4, 10$, and $20 \mu\text{l}/\text{min}$.

Again, the numerical predictions shown in Fig. 5(a) are confirmed experimentally in Fig. 5(b), for four different values of Pe . In our case, the Péclet number is only flow rate dependent, and a modification of the flow rate leads to a change in concentration profile as seen in movie S2.²⁶ For the lowest value of Pe , the concentration profile reaches a plateau after a few nodes, while higher values of Pe yield a more contrasted concentration profile across most of the ladder. Note that the concentration field for the highest flow rate displays a flat shape at the initial and final branches, thus beginning to approach the limiting case for very high Pe .

We can now use our numerical simulations to characterize the global evolution of the gradient profile with both control parameters, R/R_b and Pe . More specifically, we quantify the non-uniformity of the gradient between the branches by a contrast ratio (Figure 6), which is taken as an ansatz for the “quality” of the gradient for a given device and flow rate. This contrast ratio is defined as the root-mean-squared (rms) of the difference between the actual normalized concentration, $\tilde{C}(\tilde{x})$, and the linear gradient case, $\tilde{C}^*(\tilde{x}) = \tilde{x}$. The evolution of the contrast ratio is shown in Fig. 6(a) for various R/R_b and Pe .

The dark red canyon indicates profiles with behaviors close to a uniform gradient (Fig. 6(c)) and corresponds to gradient profiles that present high contrasts between all successive branches. The bright regions correspond to profiles that present a poor contrast between some branches and are the result of three different regimes. High Péclet numbers ($Pe > 10^4$) and low resistance ratio ($R/R_b < 10^{-2}$) correspond to a uniform flow rate distribution amongst the branches and slow diffusive effects (Fig. 6(b)). Therefore, the fluid has the behavior close to a non diffusing species regularly distributed in each side branch, with the expected distribution of a step concentration profile.

Conversely, when R/R_b is raised over 1, more than 90% of the fluid flows through the first branch and the last branch, which means that only 10% of the inlet flow goes through the rest of the branches, which cannot have a high branch concentration contrast even with rapid diffusing effects. Consequently, for high values of R/R_b , flat profiles are obtained, as shown in Fig. 6(d). Finally for Péclet numbers below 10^2 , the network geometry does not affect the concentration gradient profiles because the diffusive effects are swift enough to produce flat concentration profiles for any flow rate distribution (Fig. 6(e)).

V. EXTENSIONS AND APPLICATIONS

Several extensions of the device described above can be developed in order to apply the gradients in a range of applications and overcome some of the limitations.

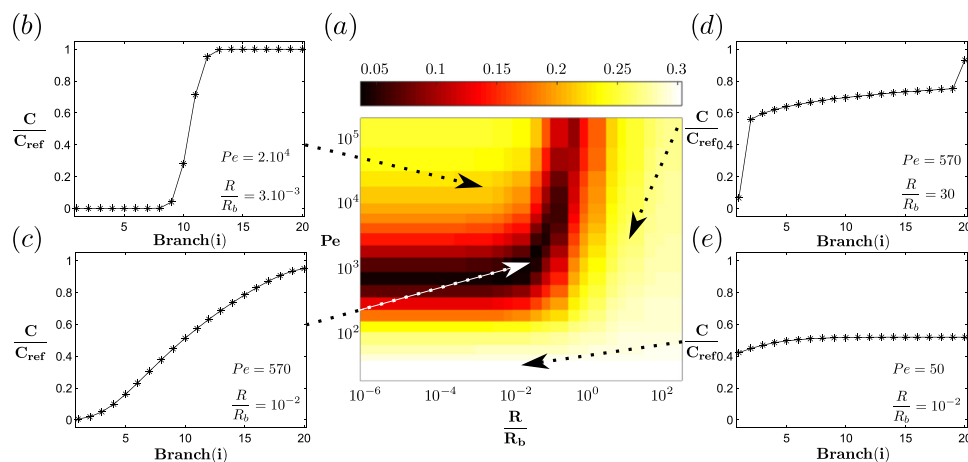


FIG. 6. (a) Map of a comparison between the concentration gradient and a constant gradient, giving the root mean square of their difference (color bar) for various values of $\frac{R}{R_b}$ and Péclet numbers Pe . (b)–(e) Concentration gradient profiles for four points of the map (a). (b) and (c) belong, respectively, to the “step” and “gradient” regimes, while (d) and (e) are examples of “flat” regime.

For instance, having a continuous flow is poorly adapted to long term observation on time scales relevant to biological experiments, which may require instead a controlled initial concentration in a closed volume. A large variety of devices already exist that maintain a concentration gradient in small chambers^{19,20} or isolate a solute in small chambers using self-digitization,²¹ but none of them combines isolation with concentration gradient. To remedy the situation, the gradient produced by the ladder network can be frozen within small chambers adjacent to the parallel channels, as shown in Fig. 7(a). Here, ten 2 nl-chambers are connected to each branch through highly resistive bypasses (Fig. 7(a) enlargement). Given sufficient time, the concentration within each chamber equilibrates with the channel to which it is connected.

The filling process of these chambers proceeds in three steps: The device is first filled with water in order to remove all the air bubbles, taking advantage of PDMS porosity. Second, a concentration gradient is applied and the chambers are progressively filled with the same concentration as in the branch they are connected to. Finally, when the gradient is completely established in every chamber, fluorinated oil (FC40 with surfactant) is flushed in the device at 345 mbar for half a second. The high resistance of the by-passes prevents the oil from entering into the chambers and allows then to be isolated. In this way, 200 independent chambers are filled with a well-controlled concentration and can be used to perform 10 repetitions at 20 different conditions in a single experiment. The stability of the concentrations in time is ensured by the low affinity of the fluorinated oils with most organic matter, making this format well adapted for protein crystallisation studies, for example, Ref. 5. The chamber concentrations agree with the model prediction (Fig. 7(b)).

A different approach is to remove the need for the ladder structure by working in a wide and thin flow chamber, as shown in Figs. 7(c) and 7(d). This format is well adapted to situations where stationary objects in the wide chamber must be submitted to variable concentrations of solute, as shown, for example, for stationary cells,^{22,23} cells in migration,⁴ or for anchored droplets.²⁴ Here, the regularity of low Re flows ensures that the fluid follows well-separated and stationary streamlines, with no lateral mixing taking place except by diffusion. In contrast,

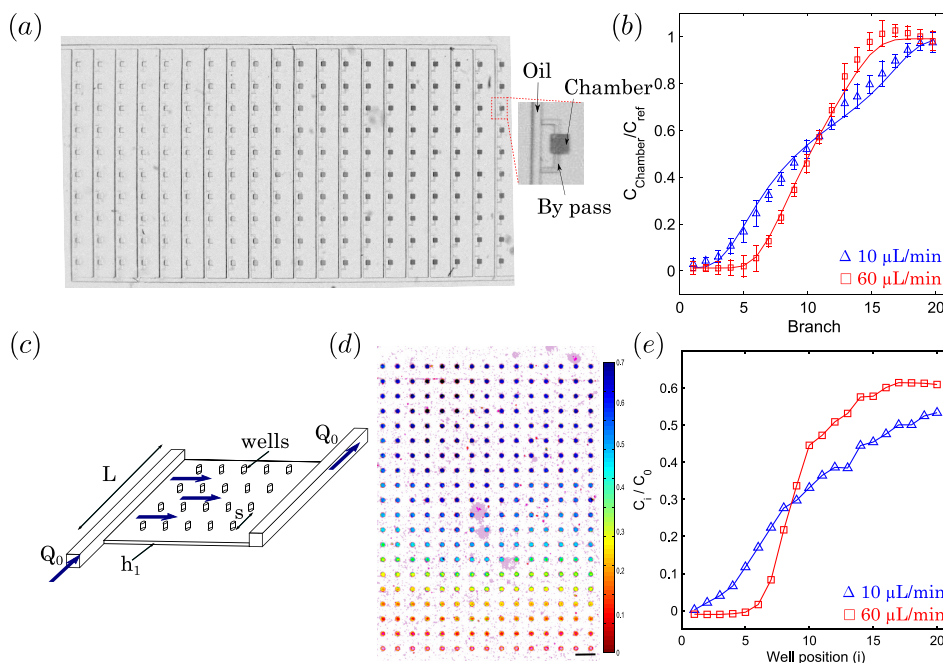


FIG. 7. Beyond the ladder network: (a) Ladder containing an array of 2 nl chambers filled with controlled and contrasted concentration. (b) Concentration profile for a global flow rate of $10 \mu\text{L}/\text{min}$ before oil flushing at 345 mbar. (c) Continuous two-dimensional implementation of the device: the ladder network is replaced by a wide and thin flow chamber. (d) False color image of the concentration profile within the chamber. Each colored dot corresponds to a well within the chamber. (e) Concentration profile for two flow rates.

the lack of parallel channels changes the underlying fluidic equilibria since the flow in these micro-Hele-Shaw cells rapidly equilibrates on a global scale to adapt to the boundary conditions. This makes the device operation more robust, therefore simpler, and improves the dynamic performance during changes of regime.

The device consists of three parts: (i) a distribution channel, 200 μm wide and 150 μm deep; (ii) a wide thin chamber placed alongside the distribution channel, having width 10 mm and height of 15 μm ; and (iii) a collection channel, whose dimensions are equal to those of the distribution channel. In the example shown in Fig. 7(d), local indentations (50 μm deep) are made in the roof of the chamber in order to improve the imaging sensitivity. As an example, a 10 mM DCPIP solution is used in a co-flow with water in the distribution channel, and a concentration gradient is observed orthogonally to the flow direction (Fig. 7(d)). Its profile depends on the flow rate in a similar fashion as the discrete case with a step concentration observed for high flow rates and a constant gradient observed for lower flow rates (Figs. 7(c) and 7(e)).

This device has been designed by understanding that the flow rate distribution plays a key role in the gradient establishment. A highly resistive chamber placed alongside the distribution channel is sufficient to create a concentration and strongly simplify the tree-like structures, commonly used in microfluidic technologies.

VI. SUMMARY AND DISCUSSIONS

This study provides new physical insights on the distribution of flows and passive tracers in a complex microfluidic geometry. We first showed that the flow is distributed in a non-trivial manner within a ladder network, with preferential paths going through the initial and final branches of the ladder (Fig. 5). This contradicts a naive application of Stokes flow principles, which would suggest that the fluid must distribute evenly in all branches, since the path from the inlet to the outlet through any of the branches would have an equal hydrodynamic resistance. Instead, we find that the extraction of fluid from the distribution channel at each node leads to a reduction of the flow rate beyond that node and thus to a nonlinear dependence of the pressure on position. The symmetric situation takes place in the collection channel, with the net effect of having a higher driving pressure across the extreme nodes and a lower driving pressure near the middle of the ladder. While the non-monotonic flow distribution is always present, a single control parameter R/R_b determines its amplitude.

Next, we considered the interplay of advection and diffusion within this geometry in setting up non homogeneous concentration profiles within the network. A second control parameter was identified, namely, the Péclet number (Pe), a measure of the relative importance of advection and diffusion in the process. Depending on those two control parameters, three broad categories of distribution profiles were identified: a flat concentration profile for low Pe or large R/R_b , a step regime for large Pe and low to moderate R/R_b , and finally a regime that displays a well-distributed gradient in a central region of this parameter space. In practice, however, any one of the three regimes may be interesting for different applications; the step regime of Fig. 6(b) allows for the exploration of a logarithmic variation in concentrations, especially in the initial regions of the device where the concentrations are low. In contrast, the flat regime of Fig. 6(d) would allow a small range to be explored in detail. The models developed here can be generalized to a wide variety of channel geometries and provide a tool to predict the distribution profile created in the device and to select the design parameters to achieve a particular profile.

Furthermore, we have shown how the concentration profile can be frozen in time within small side-chambers and how one can also completely remove the ladder network and still be able to obtain well-controlled gradients within a wide and thin cell. The case of the side chambers would allow the concentration profile to remain after the flows have been interrupted, but it requires a long setup period, determined by the time necessary to fill the most downstream chamber in the middle section of the device. The total volume required to reach this steady state was measured to be about 60 times the total volume of the ladder network. In the wall-less device case, the set-up time is much faster but the gradient requires a constant flux of the fluids.

Other methods to encapsulate the concentration variations can also be considered, for example, by coupling this gradient geometry with droplet generation, e.g., through gradients of confinement.²⁵ Such a device could potentially lead to many exciting opportunities by vastly increasing the number of parallel experiments or, alternatively, by providing the ability to perform parallel pairings of droplets while exploring a wide range of well-controlled chemical conditions.⁷

Finally, the present work focused on a model situation in which all of the branches were regularly spaced and geometrically equivalent, which significantly reduced the number of independent design parameters. The hydrodynamic resistance of the branches can however be modified, most easily by changing their lengths, in order to tune the flow rate distribution and thus the concentration profile of the solute more finely. A full design optimization is then possible to tailor the details of the conditions in the different parts of the microfluidic network.

ACKNOWLEDGMENTS

The authors acknowledge help and useful discussions with Caroline Frot, Etienne Fradet, and Morgane Grivel. The research leading to these results received funding from the European Research Council (ERC) Grant Agreement 278248 Multicell.

- ¹W. Engl, M. Roche, A. Colin, P. Panizza, and A. Ajdari, "Droplet traffic at a simple junction at low capillary numbers," *Phys. Rev. Lett.* **95**(20), 208304 (2005).
- ²M. J. Fuerstman, P. Garstecki, and G. M. Whitesides, "Coding/decoding and reversibility of droplet trains in microfluidic networks," *Science* **315**(5813), 828–832 (2007).
- ³C. N. Baroud, S. Tsikata, and M. Heil, "The propagation of low-viscosity fingers into fluid-filled branching networks," *J. Fluid Mech.* **546**, 285–294 (2006).
- ⁴C. G. Sip, N. Bhattacharjee, and A. Folch, "A modular cell culture device for generating arrays of gradients using stacked microfluidic flows," *Biomicrofluidics* **5**, 022210 (2011).
- ⁵P. Laval, N. Lisai, J. B. Salmon, and M. Joanicot, "A microfluidic device based on droplet storage for screening solubility diagrams," *Lab Chip* **7**(7), 829–834 (2007).
- ⁶L.-F. Cai, Y. Zhu, G.-S. Du, and Q. Fang, "Droplet-based microfluidic flow injection system with large-scale concentration gradient by a single nanoliter-scale injection for enzyme inhibition assay," *Anal. Chem.* **84**(1), 446–452 (2012).
- ⁷E. Fradet, P. Abbyad, M. H. Vos, and C. N. Baroud, "Parallel measurements of reaction kinetics using ultralow-volumes," *Lab Chip* **13**(22), 4326–4330 (2013).
- ⁸X. Niu, F. Gielen, J. B. Edel *et al.*, "A microdroplet dilutor for high-throughput screening," *Nat. Chem.* **3**(6), 437–442 (2011).
- ⁹M. Sun and S. A. Vanapalli, "Generation of chemical concentration gradients in mobile droplet arrays via fragmentation of long immiscible diluting plugs," *Anal. Chem.* **85**(4), 2044–2048 (2013).
- ¹⁰P. M. Korczyk, L. Derzsi, S. Jakieła, and P. Garstecki, "Microfluidic traps for hard-wired operations on droplets," *Lab Chip* **13**(20), 4096–4102 (2013).
- ¹¹O. J. Miller, A. El Harrak, T. Mangeat, J.-C. Baret, L. Frenz, B. El Debs, E. Mayot, M. L. Samuels, E. K. Rooney, P. Dieu, M. Galvan, D. R. Link, and A. D. Griffiths, "High-resolution dose-response screening using droplet-based microfluidics," *Proc. Natl. Acad. Sci. U. S. A.* **109**(2), 378–383 (2012).
- ¹²N. L. Jeon, S. K. W. Dertinger, D. T. Chiu, I. S. Choi, A. D. Stroock, and G. M. Whitesides, "Generation of solution and surface gradients using microfluidic systems," *Langmuir* **16**(22), 8311–8316 (2000).
- ¹³M. A. Holden, S. Kumar, E. T. Castellana, A. Beskok, and P. S. Cremer, "Generating fixed concentration arrays in a microfluidic device," *Sens. Actuators, B* **92**(1), 199–207 (2003).
- ¹⁴D. Irimia, S.-Y. Liu, W. G. Tharp, A. Samadani, M. Toner, and M. C. Poznansky, "Microfluidic system for measuring neutrophil migratory responses to fast switches of chemical gradients," *Lab Chip* **6**(2), 191–198 (2006).
- ¹⁵Y. Hu, X. Zhang, and W. Wang, "Simulation of the generation of solution gradients in microfluidic systems using the lattice Boltzmann method," *Ind. Eng. Chem. Res.* **50**(24), 13932–13939 (2011).
- ¹⁶S. Selimović, W. Y. Sim, S. B. Kim, Y. H. Jang, W. G. Lee, M. Khabiry, H. Bae, S. Jambovane, J. W. Hong, and A. Khademhosseini, "Generating nonlinear concentration gradients in microfluidic devices for cell studies," *Anal. Chem.* **83**(6), 2020–2028 (2011).
- ¹⁷E. Fradet, C. McDougall, P. Abbyad, R. Dangla, D. McGloin, and C. N. Baroud, "Combining rails and anchors with laser forcing for selective manipulation within 2d droplet arrays," *Lab Chip* **11**(24), 4228–4234 (2011).
- ¹⁸N. A. Mortensen, F. Okkels, and H. Bruus, "Reexamination of hagen-poiseuille flow: Shape dependence of the hydraulic resistance in microchannels," *Phys. Rev. E* **71**(5), 057301 (2005).
- ¹⁹A. Groisman, C. Lobo, H. Cho, J. K. Campbell, Y. S. Dufour, A. M. Stevens, and A. Levchenko, "A microfluidic chemostat for experiments with bacterial and yeast cells," *Nat. Methods* **2**(9), 685–689 (2005).
- ²⁰C.-W. Li, R. Chen, and M. Yang, "Generation of linear and non-linear concentration gradients along microfluidic channel by microtunnel controlled stepwise addition of sample solution," *Lab Chip* **7**(10), 1371–1373 (2007).
- ²¹D. E. Cohen, T. Schneider, M. Wang, and D. T. Chiu, "Self-digitization of sample volumes," *Anal. Chem.* **82**(13), 5707–5717 (2010).
- ²²D. Di Carlo, L. Y. Wu, and L. P. Lee, "Dynamic single cell culture array," *Lab Chip* **6**(11), 1445–1449 (2006).
- ²³P. Hersen, M. N. McClean, L. Mahadevan, and S. Ramanathan, "Signal processing by the hog map kinase pathway," *Proc. Natl. Acad. Sci. U. S. A.* **105**, 7165–7170 (2008).

²⁴P. Abbyad, R. Dangla, A. Alexandrou, and C. N. Baroud, "Rails and anchors: Guiding and trapping droplet microreactors in two dimensions," *Lab Chip* **11**, 813–821 (2011).

²⁵R. Dangla, S. C. Kayi, and C. N. Baroud, "Droplet microfluidics driven by gradients of confinement," *Proc. Natl. Acad. Sci. U. S. A.* **110**(3), 853–858 (2013).

²⁶See supplementary material at <http://dx.doi.org/10.1063/1.4932305> for supplementary movies **S1** and **S2**, which, respectively, show the flow rate and the solute distribution within the ladder network.